

Optical Coherence Tomography for Patient-specific 3D Artery Reconstruction and Evaluation of Wall Shear Stress in a Left Circumflex Coronary Artery

LAURA M. ELLWEIN,¹ HIROMASA OTAKE,^{2,3} TIMOTHY J. GUNDERT,¹ BON-KWON KOO,⁴ TOSHIRO SHINKE,³
YASUHIRO HONDA,² JUNYA SHITE,³ and JOHN F. LADISA JR.^{1,5,6}

¹Department of Biomedical Engineering, Marquette University, 1515 West Wisconsin Ave, Milwaukee, WI 53233, USA; ²Stanford University, 300 Pasteur Drive H3554, Palo Alto, CA 94305, USA; ³Kobe University Graduate School of Medicine, 7-5-1 Kusunoki-cho, Chuo-ku, Kobe 650-0017, Japan; ⁴Seoul National University College of Medicine, 101 Daehang-ro, Chongno-gu, Seoul 110-744, Korea; ⁵Department of Medicine, Division of Cardiovascular Medicine, Medical College of Wisconsin, 8701 Watertown Plank Road, Milwaukee, WI 53226, USA; and ⁶Department of Pediatrics, Division of Pediatrics, Children's Hospital and the Medical College of Wisconsin, 8701 Watertown Plank Road, Milwaukee, WI 53226, USA

(Received 3 January 2011; accepted 2 May 2011; published online 18 May 2011)

Associate Editor Stephen B. Knisley oversaw the review of this article.

Abstract—Image-based computational models for quantifying hemodynamic indices in stented coronary arteries often employ biplane angiography and intravascular ultrasound for 3D reconstruction. Recent advances in guidewire simulation algorithms and the rise of optical coherence tomography (OCT) suggest more precise coronary artery reconstruction may be possible. We developed a patient-specific method that combines the superior resolution of OCT with techniques for imaging wire pathway reconstruction adopted from graph theory. The wire pathway with minimum bending energy was determined by applying a shortest path algorithm to a graph representation of the artery based on prior studies indicating a wire adopts the straightest configuration within a tortuous vessel. Segments from OCT images are then registered orthogonal to the wire pathway using rotational orientation consistent with geometry delineated by computed tomography (CT). To demonstrate applicability, OCT segments within the stented region were combined with proximal and distal CT segments and imported into computational fluid dynamics software to quantify indices of wall shear stress (WSS). The method was applied to imaging data of a left circumflex artery with thrombus acquired immediately post-stenting and after a 6-month follow-up period. Areas of stent-induced low WSS returned to physiological levels at follow-up, but correlated with measurable neointimal thickness in OCT images. Neointimal thickness was negligible in areas of elevated WSS due to thrombus. This novel methodology capable of reconstructing a stented coronary artery may ultimately enhance our knowledge of deleterious hemodynamic indices induced by stenting after further investigation in a larger patient population.

Keywords—Computational fluid dynamics, Coronary artery reconstruction, Wall shear stress, Optical coherence tomography, Neointimal thickness, Numerical modeling.

INTRODUCTION

One in three adults in the U.S. have some form of cardiovascular disease, of which 51% suffer from coronary artery disease.³⁸ The development of stenting has revolutionized treatment of coronary artery disease, but restenosis has limited the success of bare metal stents (BMS) in ~30–51% of patients.^{13,41} Drug-eluting stents (DES) that decrease rates of restenosis were approved by the FDA in 2003 as an alternative to BMS, but may be more susceptible to late stent thrombosis²⁰ due to several factors including suboptimal endothelial cell coverage.^{10,26} Although the incidence of late stent thrombosis is just 1–2% after DES implantation, ~50–70% of these patients may experience myocardial infarction as a result.^{21,28}

Interestingly, stent implantation causes changes in vascular geometry resulting in altered local blood flow velocity and distributions of wall shear stress (WSS) that have been shown to correlate with NH³⁵ and the ability of endothelial cells to migrate onto stent surfaces.^{17,23,47} Computational fluid dynamics (CFD) simulations performed with patient-specific 3D models of the coronary arteries play a key role in quantifying indices of WSS.^{27,61} CFD models have previously been constructed using combinations of angiography and intravascular ultrasound (IVUS),^{11,27,66} but the

Address correspondence to Laura M. Ellwein, Department of Biomedical Engineering, Marquette University, 1515 West Wisconsin Ave, Milwaukee, WI 53233, USA. Electronic mail: laura.ellwein@marquette.edu

resolution of these imaging modalities (e.g., IVUS at $\sim 150 \mu\text{m}$)⁴⁵ compared to the intricacies of a stented artery may cause the loss of spatial information important for accurate model reconstruction^{7,14,46,55} and CFD analysis. Optical coherence tomography (OCT) has been used in coronary arteries since 2007 in Japan and 2010 in the United States to analyze pre-procedural lesion characteristics and the efficacy of stent implantation, offering 10 times the resolution of IVUS.^{5,8,45} Coupling OCT data with image registration and vessel reconstruction methods to create 3D coronary artery models for CFD analysis may therefore provide critical insight into the relationship between deleterious indices of WSS established after DES and their influence on thrombus or NT.

Accurately reconstructing the pullback pathway of an intravascular imaging device and subsequent orientation of images along the pathway are arguably the most critical aspects of 3D artery reconstruction using intravascular imaging modalities. Biplane angiographic imaging data was the primary source for extracting the imaging pathway in earlier studies,^{29,48,58} but its use can introduce complications such as non-orthogonal planes, an undetectable imaging wire, and the need to compensate for motion or add calibration steps beyond the clinical norm.^{6,9,24,48,50,55} The rotational orientation of images along a curved pathway estimated with points extracted from biplane angiography has also depended on the curve's functional representation, potentially causing inaccuracies with image orientation stemming from multiple functions closely representing the same curve or numerical instability of the function's derivatives.^{27,29,49,55,58,64} Further orientation issues including rotational invariance about the wire pathway and an inability to capture vessel irregularities have occurred when using angiographic images for lumen matching.^{40,48,55,64} These obstacles suggest that a method independent of biplane angiography is desirable, particularly for retrospective use.

Several recent studies have focused on predicting the pathway of a guidewire in a tortuous vessel based on the principle of minimum bending energy. Early work was conducted in the context of simulating the guidewire insertion pathway for intervention simulation^{1,25} but later studies focusing on pullback pathway reproducibility^{52,53} are more applicable to the current investigation. Applicable techniques are taken from the field of graph theory and produce a unique pathway for a guidewire that could be further used in vessel reconstruction algorithms. If this approach were implemented within a CFD modeling process it would be possible to create patient-specific models using clinical imaging data independent of the limitations mentioned above.

The objective of the current investigation was to develop an alternative method for patient-specific coronary artery reconstruction using the superior spatial resolution of OCT and a novel implementation of graph theory. Specifically, this investigation focused on OCT image segment registration onto an imaging wire pullback pathway determined by implementing Dijkstra's algorithm on a graph representation of the left circumflex artery (LCX). The method was applied in a retrospective manner using computed tomography (CT) and OCT data of a single patient's LCX acquired immediately after stenting ("post-stent") in the presence of thrombus, and again after a 6-month period ("follow-up"). These arterial reconstructions were used with CFD to demonstrate the utility of quantifying indices of WSS for comparison with NT measured from OCT images.

METHODS

The methods developed to complete our objective are divided into four processes as illustrated by the workflow displayed in Fig. 1: Data Collection, Model Construction, Simulation, and Results Quantification. Process 2, Model Construction, consists of five stages labeled A. Image processing, B. Wire pathway reconstruction, C. Segment registration, D. Model assembly, and E. Stent implantation. Stage 2B is the focus of this investigation and consists of four steps that are completed before Stage 2C commences.

Data Collection

This investigation was approved by the ethical committee of Kobe University and Institutional Review Board at Marquette University. Informed consent was obtained for the use of data in this case study. Coronary angiography and OCT imaging were performed immediately and 6 months after DES implantation as previously reported.⁴⁶ OCT images were acquired with a time-domain M2 OCT Imaging System (LightLab Imaging Inc., Westford, MA, USA) having axial and lateral resolutions of 15 and 25 μm , respectively.⁵ A 0.016-inch OCT fiber-optic imaging wire with a photodetector at its tip (ImageWire, LightLab Imaging, Westford, MA, USA) was advanced to the distal end of the stented lesion through an occlusion balloon catheter (HeliosTM, LightLab Imaging Inc., Westford, MA, USA). The occlusion balloon was inflated to 0.5 atm at the proximal site of the stented lesion, and Lactated Ringer's solution was infused into the coronary artery from the distal tip of the occlusion balloon catheter at 0.5 mL/s to flush the area clear of blood. The entire stented length was then

Methods Workflow

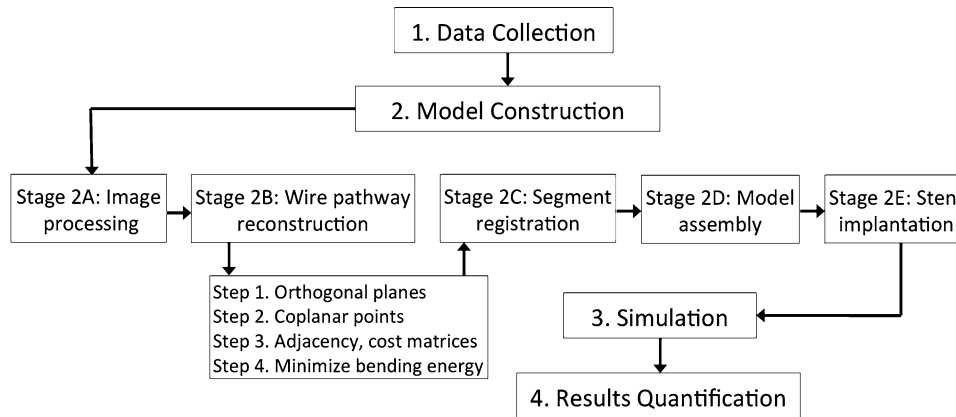


FIGURE 1. Diagram of the workflow developed and implemented for the current investigation. The workflow is divided into four processes including 1. Data Collection, 2. Model Construction, 3. Simulation, and 4. Results Quantification. Process 2, Model Construction, consists of five stages labeled A. Image processing, B. Wire pathway reconstruction, C. Segment registration, D. Model assembly, and E. Stent implantation. Stage 2B is the focus of this investigation and consists of four steps that are completed before Stage 2C commences.

imaged using an automatic pullback speed of 1 mm/s at 15 frames/s. The lesion was also evaluated before stent implantation with a 64-slice multidetector CT scanner resulting in a voxel size of $0.39 \times 0.39 \times 0.5$ mm (Aquillion 64, Toshiba Medical Systems, Tokyo, Japan). Volume-rendered CT data and a corresponding longitudinal OCT cross-section are shown in Fig. 2.

Analysis of OCT images was performed by an independent observer who was blinded to clinical presentation and lesion characteristics. Cross-sectional OCT images were quantified at 1-mm intervals. Lumen area was determined by tracing the leading edge of the blood/intima border. Stent area was delineated by first marking the center of each stent strut, then automatically interpolating between strut locations using the integrated Lightlab image analysis software.⁴³ These tracings (hereafter referred to as segments) are marked by white and cyan contours, respectively. Intracoronary thrombus was defined as a protruding mass beyond the stent strut into the lumen with significant attenuation behind the mass.⁴⁶

Model Construction

The model construction process contains five distinct stages: A. Image processing, B. Wire pathway reconstruction, C. Segment registration, D. Model assembly, and E. Stent implantation. The first four stages are common to both the post-stent and follow-up OCT data sets, but are implemented separately on each. The final stent implantation stage is applicable to the post-stent data only. Resulting computational models represent the LCX from ~10 mm proximal to

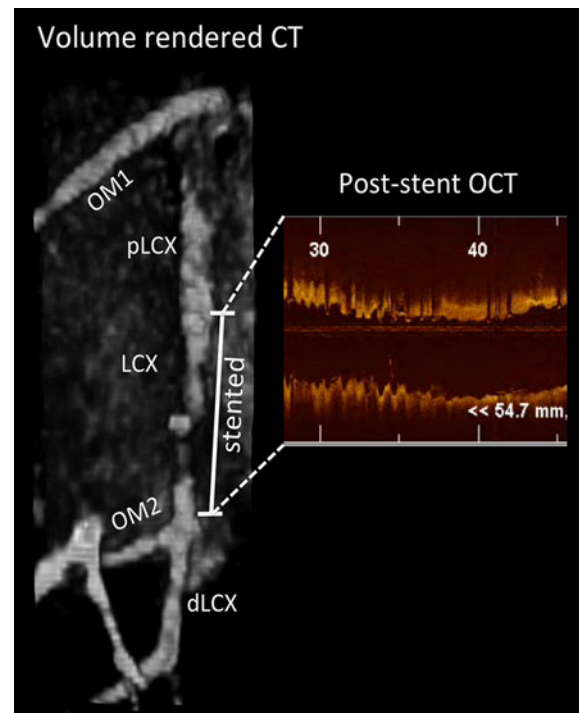


FIGURE 2. Left: Volume rendering of computed tomography data obtained from the left circumflex coronary artery (LCX) prior to stent implantation. The thrombus, evident by a lack of bright blood flow in the LCX, is located in the distal half of the stented region. Right: Longitudinal view of OCT data from post-stent assessment. A similar image was also acquired during the follow-up assessment. OM1: first obtuse marginal artery. OM2: 2nd obtuse marginal artery. pLCX: LCX proximal to the stented region. dLCX: LCX distal to the stented region and the OM2.

the stent (just distal to the 1st obtuse marginal artery) to ~10 mm distal to the bifurcation at the second obtuse marginal (OM2), including portions of both

bifurcating arteries. The distal end of the stent was located just proximal to the OM2 bifurcation. Specific computations used for these stages discussed in detail below were performed in Matlab (MathWorks; Natick, MA) unless otherwise specified.

Stage A. Image Processing

OCT images were processed in Matlab using algorithms provided in the Image Processing Toolbox. Images were converted to grayscale, masked to remove measurement markings, and thresholded relative to the color of segments, resulting in binary images of the original OCT images with a black background and segment pixels isolated in white. Pixels were converted to Cartesian coordinates with the z -coordinate for each image segment representing its pullback distance. Segments were then aligned vertically in succession and spaced using the known pullback rate of 15 frames/mm, resulting in a vertical stack of OCT segments positioned with the z -axis intersecting each segment at its centroid.

Stage B. Wire Pathway Reconstruction

During OCT, images are acquired orthogonal to the photodetector at the tip of the imaging wire and do not necessarily lie on the vessel centerline, thus requiring determination of the wire pullback pathway to ensure precise segment registration. As discussed in the Introduction, the wire follows the straightest pathway within the tortuous vessel (i.e. it minimizes its total bending energy) provided the vessel tortuosity is above a value of 1.2, defined as the ratio between the total centerline arc length and the direct distance between centerline start and end points.⁵³ The pathway is therefore determined by framing the problem as an optimization for which both a spatial network representation of the set of possible wire pathways and an associated graph representation are required. This network-graph dual representation is adopted from Schafer *et al.*⁵³ and is demonstrated below for a simple case.

Demonstration of Concept

The simple case of a vessel comprised of three orthogonal planes P_i and two points P_{ij} per plane can be expressed using the network-graph dual representation introduced above. Sets of coplanar points are connected such that a joint $\varepsilon = (v_1, v_2)$ at a candidate point is defined to be a composition of two vectors $v = a...l$ connecting the point with candidate points in successive proximal and distal sets of points (Fig. 3a). For example, $v = e$ and $v = k$ connect points P_{12}, P_{22}, P_{32} in consecutive planes $P_1, P_2,$ and P_3 . This network of joints connected by vectors encompasses a spectrum of possible wire pathways, and the wire pullback

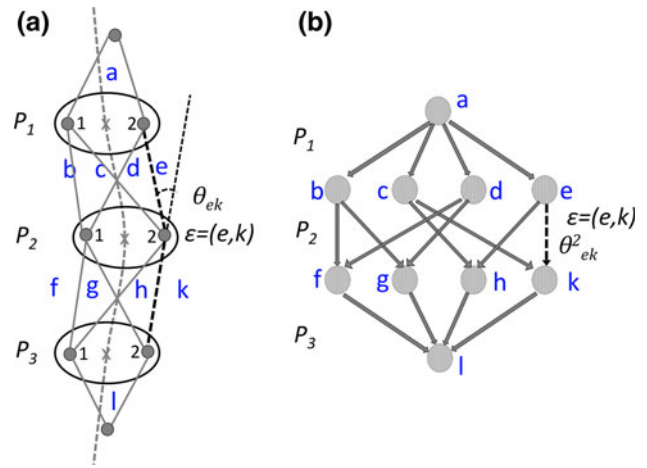


FIGURE 3. (a) Network and (b) graph representations of a simple case vessel with three planes and two points per plane. (a) Vectors in the network diagram are labeled as $a...l$ and colored light grey. Joints ε are connections between two vectors and colored dark grey. The joint $\varepsilon = (e, k)$ is indicated by dotted lines with its angle measurement θ_{ek} . Segments are shown as black ellipses and the centerline is dotted grey, passing through centroids marked with a grey 'x'. (b) Vertices and edges of the graph correspond to vectors and joints of the network, with vertices labeled $a...l$ in light grey and edges in dark grey. The weight θ_{ek}^2 is assigned to edge $\varepsilon = (e, k)$. Vertices a and l are added to the graph to ensure single source and destination vertices for the shortest path algorithm. All edges adjacent to these vertices a and l are given equal weights because these vertices lack physical meaning but are included for completeness.

pathway as determined by the optimization algorithm passes through one point in each set of points on each plane starting at one end of the vessel.

The network of possible pathways is further represented for the simple case as a directed graph $G = (V, E)$, with joints now indicated as edges (E) and the connecting vectors as vertices (V) (Fig. 3b). Graph vertices, $v \in V$, correspond to network vector connections between joints that comprise the possible wire pathways, labeled as $a...l$ as were the vectors of the network. Graph edges, $\varepsilon \in E$, represent the joints connecting vectors between P_i , e.g., $\varepsilon = (e, k)$. Representing the network as a graph allows us to implement a minimization algorithm that does not search over all connections between all candidate points, but instead considers only connections that make valid pathways based on previous connections and pathway direction. In the simple case, $a-e-k-l$ is a valid pathway but $a-e-g-l$ and $l-k-e-a$ are not. The vertices a and l are added to ensure single source and destination vertices for the graph and vectors defining joints for the first and last planes of the network. The resulting start and end points created in the network are outside of the planes and do not affect the minimization.

The pathway with minimum bending energy composed of an ordered set of joints is determined by

minimizing total bending energy, $U_{\text{total}} = \sum U_{\text{bend}}$, over all pathways. Bending energy, U_{bend} , at each joint is assigned as the weight for each corresponding graph edge. It is defined as $U_{\text{bend}} = (1/2)C\theta^2$ according to an adaptation of Hooke's law for molecules as is customary in previous studies,^{1,4} where θ is the supplement of the angle of the joint (i.e. an angle of 0 is a straight joint) and the parameter C comprises several constant spring parameters. The minimization problem is independent of the value of any multiplied constants, thus the contribution of the constants is negligible and the square of the joint angles, θ^2 , were assigned as edge weights. The angle θ was calculated from the standard cosine formula, e.g., $\theta_{ek} = 180 - \cos^{-1}(v_e \cdot v_k) / (|v_e||v_k|)$ between vectors e and k (see Fig. 3b).

The minimum path of the graph is calculated with the aid of numerical methods. These methods require an adjacency matrix with ones indicating a directed edge between two vertices and zeros indicating no edge, as well as a cost matrix with the calculated weights that are assigned to each edge included as matrix entries where ones are located. Rows of the matrix indicate the starting vertex and columns the ending vertex for each edge. Figure 4 shows the matrices that correspond to the simple case detailed in Fig. 3 with entries for edge $e-k$ highlighted. The first row, last column, and block matrices in the interior have a structure directly related to the network, e.g., the 4×4 block matrix for the simple case indicates the 8 joints on plane P_2 . All edges adjacent to vertices a and l are given equal weights because these vertices lack physical meaning but are included for

completeness. The output of the numerical method is the succession of joints that make up the minimum bending energy pathway.

Implementation

The imaging wire pathway for the coronary vessel in this investigation was determined using the procedure outlined above. OCT image segments processed in Stage A were used to determine the necessary orthogonal planes and sets of coplanar candidate points because they contain 2D lumen centroid and wire position information that lends greater precision to the analysis. The steps for obtaining the imaging wire pathway are listed below followed by a detailed exposition:

Step 1. Identify planes orthogonal to the vessel centerline using CT data and OCT segments.

Step 2. Identify sets of coplanar candidate points lying on the orthogonal planes that will comprise the joints of the possible wire pathways.

Step 3. Formulate adjacency and cost matrices that describe the graph of the network formed by the sets of coplanar candidate points.

Step 4. Apply Dijkstra's algorithm to the graph using its adjacency and cost matrices to obtain the pathway of minimum bending energy.

Step 1. Identify orthogonal planes. As a first approximation of OCT segment registration and to designate orthogonal planes within the imaged region, segments are placed longitudinally on the LCX centerline at their centroids. The centerline was generated from the CT data using the open-source software packages ITK-Snap (www.itksnap.org) and VMTK (www.vmtk.org) as previously described.³ Briefly, 3D segmentation in ITK-Snap was performed using intensity regions with lower threshold of 175 and no upper threshold, and snake propagation of 25 iterations. The length of the centerline used for the analysis extended from the 1st obtuse marginal artery to approximately 60 mm distal to the OM2. Longitudinal spacing along the centerline was ensured by first anchoring image segments acquired at two landmarks, the OM2 and a smaller (side) branch originating from the middle of the stented region, with lumen centroid coordinates at these positions extracted using ITK-Snap. Remaining segments were distributed according to the wire pullback speed.

Segments (S) are transformed from the vertical (v) stack to the centerline (c) by using the inverse of the rotation matrix (R) that aligns the centerline tangent (t) at each longitudinally spaced centerline registration point with the z -axis of the vertical stack (Fig. 5). This pair of operations is represented mathematically by the equations $Rt_c = t_v$ and $R^{-1}S_v = S_c$, where R is constructed such that the x and y coordinates of

Adjacency matrix										Cost matrix											
	a	b	c	d	e	f	g	h	k	l											
a	0	1	1	1	1	0	0	0	0	0	0	θ	θ	θ	θ	0	0	0	0	0	0
b	0	0	0	0	0	1	1	0	0	0	0	0	0	0	0	θ	θ	0	0	0	0
c	0	0	0	0	0	0	0	1	1	0	0	0	0	0	0	0	0	θ	θ	0	0
d	0	0	0	0	0	1	1	0	0	0	0	0	0	0	0	θ	θ	0	0	0	0
e	0	0	0	0	0	0	0	1	1	0	0	0	0	0	0	0	0	θ	θ	0	0
f	0	0	0	0	0	0	0	0	0	1	0	0	0	0	0	0	0	0	0	0	θ
g	0	0	0	0	0	0	0	0	0	1	0	0	0	0	0	0	0	0	0	0	θ
h	0	0	0	0	0	0	0	0	0	1	0	0	0	0	0	0	0	0	0	0	θ
k	0	0	0	0	0	0	0	0	0	1	0	0	0	0	0	0	0	0	0	0	θ
l	0	0	0	0	0	0	0	0	0	0	0	0	0	0	0	0	0	0	0	0	0

FIGURE 4. Examples of adjacency and cost matrices for a simple case vessel with three planes, two points per plane (see Fig. 3), required for the numerical implementation of a shortest path algorithm. Rows indicate the starting vertex and columns the ending vertex for each edge. The 4×4 matrix in the black box indicates the 8 joints found on plane P_2 , showing also the structure of the block matrix exploited for automated matrix construction for a larger network. The smaller dotted box highlights the $e-k$ joint/edge with weight θ_{ek} .

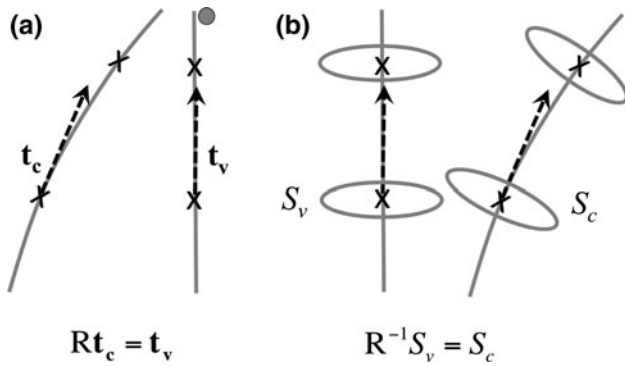


FIGURE 5. Diagram of OCT segment placement onto vessel centerline. (a) A matrix R is calculated at each longitudinally spaced centerline registration point that rotates centerline tangents t_c to align with the z -axis of the vertical stack such that the x and y coordinates of the resulting t_v equal 0. (b) The matrix R^{-1} is applied to the segments S_v in the vertical stack, creating orthogonal segments S_c on the vessel centerline.

t_v equal 0. The resulting segments S_c are orthogonal to the vessel centerline, with segment normals originating at the segment centroid aligned with centerline tangents. S_c determines orthogonal planes P_i in the imaged region used for the remaining steps. In addition, a sufficient number of orthogonal planes proximal and distal to the region imaged by OCT were calculated using centerline tangents to ensure accuracy while minimizing computation time,⁵³ resulting in a total of 33 planes.

Step 2. Identify sets of coplanar points. Orthogonal planes identified in the previous step were used to define sets of 13 coplanar candidate points, $P_{ij}, j = 1 \dots 13$. Proximal and distal to the region imaged by OCT, each set of P_{ij} included the centroid, 4 points equally spaced at $1/3$ radius from the centroid, and 8 points equally spaced $2/3$ radius from the centroid (Fig. 6a), in order to span the cross-section. For the planes in the imaged region, the distance between each segment's centroid and wire location was known by direct measurement from the OCT images. Therefore the P_{ij} were created within the plane segments using 13 equally spaced points surrounding the centroid at a radius equal this distance (Fig. 6b). Finally, for the two segment planes anchored at branch landmarks, coordinates for the wire points were explicitly determined from ITK-Snap, similar to what was done in Step 1 for anchoring centroid coordinates. Note that aside from the two anchored segments, rotational positioning of remaining segments is unknown at this step, thus the need for P_{ij} that circumferentially span the lumen cross-section.

Step 3. Formulate adjacency and cost matrices. In this investigation, adjacency and cost matrices were generated using a custom automated script that exploited the fact that the same number of joints exist on each plane. Matrices were square with size $(N - 1)M^2 + 2$, where N is the number of defined planes and M is the number

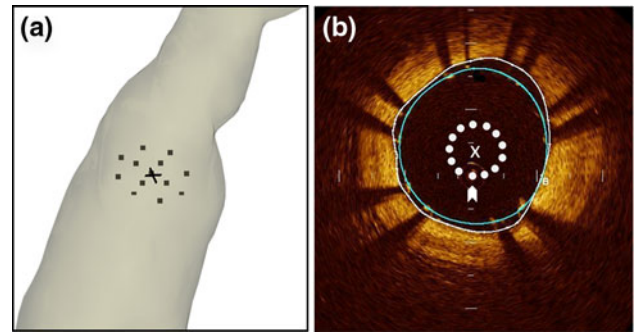


FIGURE 6. (a) Representative orthogonal set of 13 coplanar wire pathway candidate points P_{ij} proximal to the imaged region, including the point at the lumen centroid marked with a black 'x', 4 points equally spaced at $1/3$ radius from the centroid, and 8 points equally spaced $2/3$ radius from the centroid. Points are shown within a volume rendering of CT data used for centerline determination. (b) Representative post-stent OCT image with lumen (white) and stent (cyan) segment showing locations of 13 P_{ij} marked with white dots and lumen centroid with a white 'x'. Points are equally spaced surrounding the centroid at a radius equal to the distance between the centroid and wire location at the image center (white arrow).

of points per plane (33 and 13 for this investigation, respectively). Similar to what was shown in Fig. 4, the first row of the adjacency matrix consists of one zero, M^2 ones, and the remaining entries as zeros, while the last column begins with zeros and ends with M^2 ones and one zero. The $(N - 2)M^2$ columns prior to the last column consist of block matrices of size M^2 . The fixed point in each of the two anchor planes described in Step 2 was treated as if it was 13 identical points in order to simplify matrix generation.

Step 4. Solve shortest path problem to minimize bending energy. A validated numerical Dijkstra's algorithm script (MathWorks, www.mathworks.com) was implemented in Matlab to evaluate the shortest path from the source to the destination vertex using the adjacency and cost matrices determined in Step 3. The output of the script is the succession of joints, and thus the candidate points, that make up the minimum bending energy pathway. To refine the location of these points, Dijkstra's algorithm was implemented a second time on a new set of 13 candidate points within each plane that included each respective point found from the first implementation of the algorithm. The encompassing radius for the new set of candidate points was less than $1/3$ of the lumen radius at each location to ensure the new points remained within the vessel. The final set of pathway points was interpolated to the nearest 0.1 mm to determine the entire pathway.

Stage C. Segment Registration

Registration of OCT segments on the wire pathway was performed in a manner similar to what was done

to identify orthogonal planes as described in Step 1 of Stage B, noting that the wire pathway passes through the center of each image. Segments from images at the OM2 and side branch were anchored according to the fixed coordinates of where the wire passes through each segment. Remaining segments were spaced longitudinally by their image centers along the wire pathway determined in Stage B according to wire pullback speed. Segments are transformed onto the wire pathway by applying the inverse of a new rotation matrix that aligned the tangent at each longitudinally spaced pathway registration point with the z -axis of a vertical stack of the images. As a result, segment normals originating where the wire intersects the segment plane align coincident with pathway tangents, thus placing segments orthogonally on the wire pathway at these intersection points. To account for rotational orientation, each image segment was rotated within its orthogonal plane such that the wire pathway point (image center), the segment centroid, and the point of intersection between the centerline and the orthogonal plane were aligned. Final segment alignment for segments in the stented region is shown in Fig. 7a.

Stage D. Model Assembly

To be consistent across the two data sets for the single patient and to include the OM2 bifurcation in the models of the flow domain, the regions proximal and distal to the stented regions were created with the CT data in ITK-Snap and combined with the stented region to form the entire vessel. These regions include the LCX proximal to the stented region (pLCX) and the bifurcation of the distal LCX (dLCX) and OM2. Evaluation of the flow waveform used as the inflow boundary condition indicated that the pLCX should be extended to accommodate an entrance length of 11 mm and bifurcating artery branches were similarly extended. 3D segmentation in ITK-Snap was performed using intensity regions with lower thresholds of 125 (OM2) or 175 (pLCX, dLCX) and no upper threshold. Snake propagation continued for 10 (OM2) or 25 iterations (pLCX and dLCX). 3D representations of the pLCX and dLCX were queried using customized scripts in Matlab to create orthogonal segments defining the vessel lumen. These segments were imported into the open-source software Simvascular (<https://simtk.org/home/simvascular>) together with the processed segments from the stented region registered on the wire pathway. The total collection of segments was then lofted and blended to form a Parasolid model (Siemens, Plano, TX) of the full flow domain. The follow-up flow domain model reconstructed from lumen segments in follow-up OCT images was complete after these first four steps described above (Fig. 7b).

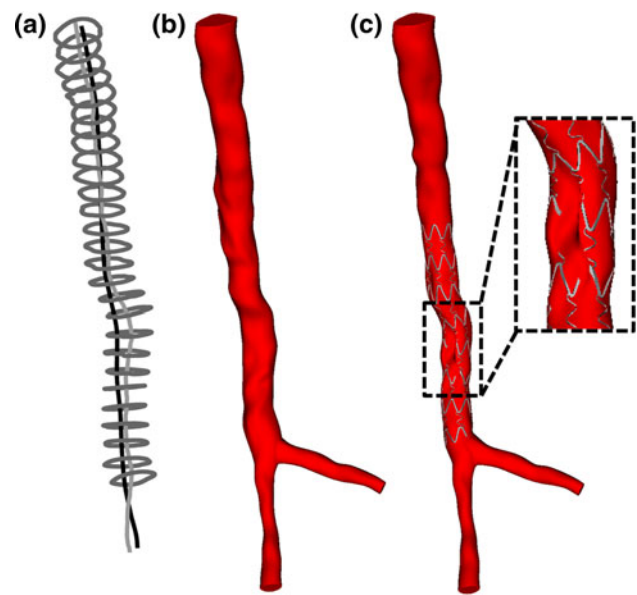


FIGURE 7. (a) Final alignment of OCT segments in the stented region (dark grey) in 3D space with the centerline in light grey and the wire pathway in black. (b), (c) Computational solid model representations of vessel flow domains for the follow-up and post-stent phases, respectively. The thrombus area is outlined by the black dashed box.

Stage E. Stent Implantation

To create the post-stent LCX flow domain model, a stent was virtually implanted proximal to the dLCX/OM2 bifurcation using a method similar to that described by Gundert *et al.*,¹⁶ which was modified to account for a patient-specific flow domain that may contain plaque or thrombus in the stented region (Fig. 8). Briefly, a first-generation drug-eluting CYPHER[®] stent (Cordis Corporation, Bridgewater, NJ) that was used clinically for this patient was created in Solidworks (Solidworks Corp. Concord, MA) from the known geometry of the stent but with accentuated radial thickness. Separate solid models of the vessel lumen and the lofted outer surface of the stent were constructed from the white and cyan segments of the OCT images (Fig. 8a), respectively, using the procedure described in Stages A-D above (Figs. 8b and 8e). The stent radial thickness was then subtracted from the solid model of the lofted stent to create a thinner lofted stent model (Fig. 8b). Subtracting the thinner lofted stent model from the thick stent yielded a patient-specific stent model that mimicked the inner surface of the stent (Figs. 8c and 8d). The final subtraction of this stent model from the lumen model (Fig. 8f) generated the flow domain used for subsequent CFD simulations (Figs. 8g and 7c). Because the stent and lumen are created separately, thrombus and other features of the vessel wall that partially cover stent struts are represented in the resulting flow domain (dashed box, Fig. 7c).

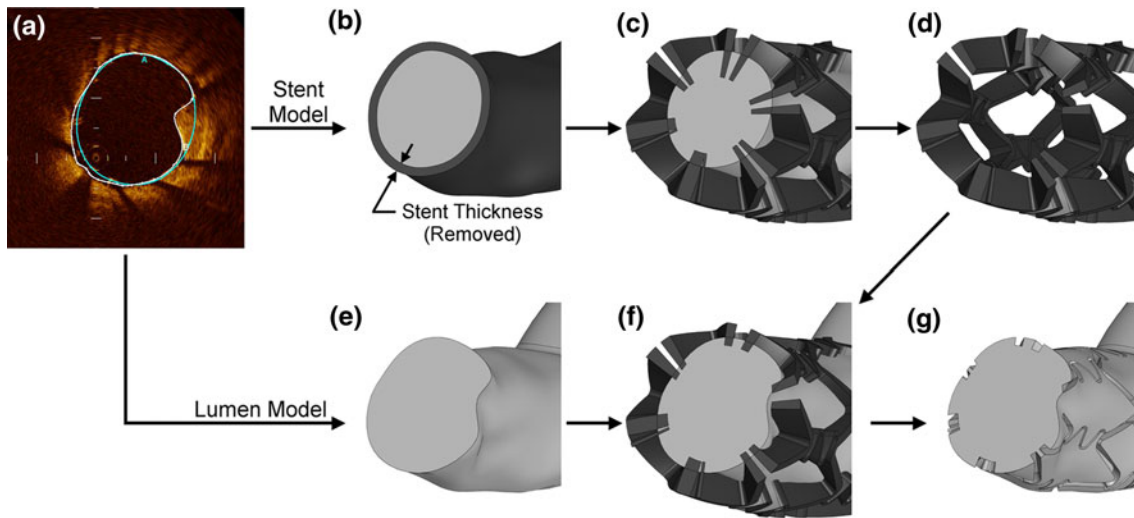


FIGURE 8. Method of virtual stent implantation. Solid models of the outer surface of the stent (b) and vessel lumen (e) were lofted from the white and cyan segmentations of the OCT images (a). The stent radial thickness was subtracted from the model of lofted stent segmentation (b), which was subsequently subtracted from a thick stent model (c) to create a patient-specific stent model (d). Subtracting the patient-specific stent model (d) from the lumen model (e) as shown in (f) generated a computational representation of the blood flow domain (g).

Simulation: Boundary Conditions and Parameters

Post-stent and follow-up vessels were subjected to a canine pulsatile blood flow waveform contour obtained from the left anterior descending coronary artery³² similar in size to the current patient's LCX, and with features including Reynolds and Womersley numbers which have allowed the waveform to be previously applied in many computational studies.^{31,33,34,69} Based on the patient's cardiac output (Table 1), mean blood flow for the LCX was determined assuming the coronary arteries receive 5% of cardiac output, 84% of which is allocated to the left main coronary artery from which the LCX receives 33%.³⁶ The flow waveform contour was then scaled to the mean LCX flow and imposed at the model inflow face as a time-varying Womersley velocity profile using Simvascular. Distributions of blood flow to the OM2 and dLCX branches (46 and 54%, respectively) were calculated by assuming WSS is the same for both arteries. Blood was assumed to behave as a Newtonian fluid (4 cP) with a constant density (1.06 gm/cm³).

The physiologic influence of the arterial tree distal to the flow domain was modeled at vessel outlets using a three-element Windkessel representation with parameters R_c , C , and R_d .⁶³ R_c is the characteristic impedance representing the resistance, compliance and inertance of the proximal artery of interest, C is the arterial capacitance and accounts for the sum of the compliance of arteries beyond the model outlets, and R_d describes the distal resistance in the absence of ventricular contraction.⁶⁸ Collectively, R_c , R_d and the time-varying resistance to blood flow resulting from

TABLE 1. Patient data used to establish boundary conditions for CFD simulations.

Data	Value
Age (years)	65
Height (inches)	64.3
Weight (lbs)	108.7
Heart rate (bpm)	82
Blood pressure (mmHg)	131/68
Cardiac output (L/min)	4.21
Reynolds number	76
Womersley number	2.16

ventricular contraction can be calculated as the ratio of mean BP and mean flow. In the absence of ventricular contraction using the impulse response method of Van Huis *et al.*, R_c and R_d constitute the zero hertz impedance, Z_0 , that is $\sim 38\%$ (range 22–65%) less than the total resistance value.⁶² Thus, the ratio of mean BP and mean flow mentioned above was scaled by 65%, for the current work to be within this range presented by Van Huis *et al.* and consistent with our previous results using these methods.⁶⁹ R_c is reflective of the average impedance of frequencies above 7 Hz and can be calculated as $C_{ph}\rho/(\pi r^2)$ where c_{ph} is the wave speed, ρ is the blood density, and r is the vessel radius.⁶² Applying a wave speed of 6.77 m/s for the canine LCX¹⁵ the R_c values for the outlet branches were determined and R_d was calculated as the difference between Z_0 and R_c . The capacitance at each outlet was determined prior to running simulations using an automated Matlab program that determines pulse BP based on an inflow waveform, the calculated

R_c and R_d values and an *a priori* estimate for C .⁵⁶ The capacitance was then adjusted to match the desired systolic and diastolic BP values using this pulse pressure method.⁵⁷

Anisotropic meshes with unstructured tetrahedral elements were created for each model using an automated mesh generation program (MeshSim, Simmetrix, Clifton Park, NY) capable of local adaptation.^{42,51} The initial meshes were generated with maximum element edge equal to the width of a stent strut. Successive meshes were adaptively refined after each pulsatile simulation using a minimum edge size equal to one-fourth of the strut width in order to place more elements where they are most needed within the flow domain while inserting fewer elements where a coarse density is sufficient. Simulations were performed with the commercially-available flow solver, LesLib (Altair Engineering Inc., Troy, MI), which uses a stabilized finite element method to solve equations for conservation of mass (continuity) and balance of fluid momentum (Navier-Stokes). Three cardiac cycles ensured simulation convergence with maximum difference in BP between equivalent time points in successive cardiac cycles < 1 mmHg. Simulation results were considered to be independent of mesh size when the change in TAWSS between successive meshes at chosen proximal and distal intrastrut regions was $< 6\%$.^{31,44}

Results Quantification

TAWSS and oscillatory shear index (OSI) were calculated as in previous studies^{19,60} and visualized using ParaView (www.paraview.org). OSI is a measure of WSS directionality in which lower OSI values indicate WSS is oriented predominantly in the primary direction of blood flow while a value of 0.5 is indicative of bi-directional WSS with a time-average value of zero. It has been shown that low TAWSS (< 4 dyn/cm²) and high temporal oscillations quantified by OSI are associated with NT in the coronary arteries,^{35,39,65} therefore the vessel surface exposed to TAWSS below this value was used to quantify the impact of the implanted stent and changes at follow-up. Indices of WSS were also displayed in an unwrapped 2D configuration to more clearly visualize differences from the post-stent to follow-up periods and facilitate querying of results at similar locations. In addition, a continuous NT measurement was quantified from the follow-up OCT images by subtracting the lumen segment from the stent segment at equivalent circumferential locations measured relative to the lumen centroid to obtain the perpendicular radial distance between the segments. NT was plotted with TAWSS results queried at post-stent along planes equivalent to those at which the follow-up OCT images were acquired.

RESULTS

Vessel Reconstruction

Two patient-specific computational models were created from OCT images using the methods described in “Methods” section; one model of the flow domain immediately post-stenting (Fig. 7c) that preserves the thrombus remaining in the lumen, the other of the flow domain after a 6-month follow-up period (Fig. 7b) during which the thrombus substantially decreases. Total centerline length from the pLCX to the dLCX used in this methodology was 107 mm and the direct distance from the start to the end points of the centerline was 77 mm, giving a tortuosity of ~ 1.4 , sufficient for implementation of the algorithm. The stented model includes replication of the stent placement according to vessel geometry, including flexing that follows vessel curvature, rotational orientation based on information from OCT images at branch landmarks, and a slight protrusion of the stent into the lumen at the bifurcation.

Indices of Wall Shear Stress

Distributions of TAWSS and OSI for the post-stent and follow-up cases are shown in Fig. 9. Areas of high TAWSS (> 100 dyn/cm²) occur both at the thrombus (dashed box, Figs. 9a and 9b) and at narrower regions of the vessel. The percentage of the vessel surface exposed to low TAWSS (< 4 dyn/cm²) was 11% in the post-stent model likely due to areas of low WSS found next to stent struts, but 3% in the follow-up model and limited to areas of localized curvature (Fig. 9c). Although regions of high OSI near stent struts are present at post-stent, high OSI remaining at follow-up is limited to areas of curvature (Fig. 9d), likely due to neointimal coverage on stent struts preventing flow stagnation.

TAWSS extracted lengthwise along the stented portion of the LCX at four circumferential locations is shown in Fig. 10. Each of the four post-stent locations quantified shows regions of low TAWSS < 4 dyn/cm² occurring approximately every 4 mm, corresponding to areas adjacent to struts. Conversely, TAWSS returned to physiological levels > 10 dyn/cm² at most locations by follow-up. However, on the myocardial wall at 24 mm (see also Fig. 9c) and the epicardial wall at 20 mm, two areas of vessel curvature, TAWSS remains below 4 dyn/cm². In addition, high TAWSS in intrastrut regions at post-stent decreased markedly at follow-up. TAWSS at one thrombotic and one non-thrombotic longitudinal location encircling the circumference of the vessel is shown in Fig. 11 for both data sets. The location of thrombus (20.5 mm) has one region of TAWSS > 100 dyn/cm² with the remainder

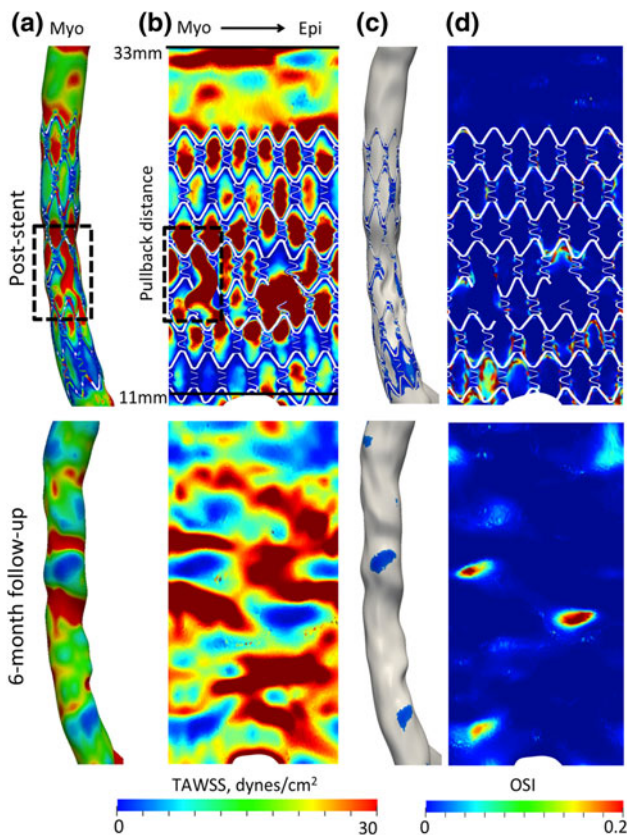


FIGURE 9. Comparison of TAWSS and OSI on the LCX proximal to the OM2 bifurcation under post-stent and follow-up conditions. From left to right: (a) 3D myocardial view of TAWSS on the LCX, with the thrombus area outlined by the black dashed box. (b) Unwrapped 2D view of all surfaces. (c) 3D myocardial view of surfaces exposed to TAWSS < 4 dyn/cm². (d) Unwrapped view of OSI.

of the vessel at that location under 50 dyn/cm². In contrast, the example of a non-thrombotic region (16 mm) shows several locations of moderate TAWSS 60 – 80 dyn/cm² resulting instead from vessel narrowing. Superimposed is a moving average representation of the post-stent TAWSS calculated with an averaging window size equal to the intrastent dimension, which appears to closely resemble the plot of follow-up TAWSS.

For this single patient, continuous NT extracted from OCT images acquired at follow-up appears to correlate with post-stent TAWSS from CFD simulations at corresponding circumferential locations (Fig. 12). For example, two cross-sections in non-thrombus areas show measurable growth at specific locations with TAWSS < 4 dyn/cm². In contrast, the cross-section at the proximal end of the thrombus with high TAWSS > 80 dyn/cm² shows minimal NT, as does the high TAWSS region of the non-thrombus mid-high range cross-section.

DISCUSSION

The current investigation describes a new method of 3D coronary artery reconstruction for use in creating patient-specific CFD models that serves as an alternative to earlier methods in several distinct ways. The most evident of these is the use of OCT to provide highly resolved spatial information and improved morphological detail in regions of thrombus within stented coronary arteries as compared to IVUS for 2D image acquisition or CT angiography for 3D segmentation and reconstruction. In conjunction with coronary artery reconstruction we also provide an extension of a previously documented method for virtual stent implantation that preserved important elements of LCX geometry and pathology in the post-stent model. Perhaps most impactful, however, is the process introduced for determining the OCT imaging wire pathway for image segment registration implemented with graph theory techniques that alleviate issues inherent in the common practice of biplane angiography discussed in more detail below.

Comparison with Biplane Angiography

Orthogonal biplane angiographic images are commonly used to determine the intravascular imaging pathway and/or the vessel lumen itself. While biplane angiography is a common clinical practice prior to percutaneous coronary interventions, potential issues include non-orthogonality of views, alternating timing of data acquisition between planes, cardiac/respiratory movement, imaging device visibility, and general image quality.^{55,58} In contrast, exploiting the principle of minimum bending energy using the methods described here allows for pathway determination for retrospective studies in which biplane angiography is either unavailable or presents the issues discussed above. When points extracted from biplane angiography are fit to a curve using a variety of functional forms, multiple possible rotational orientations may result from problems with numerical instability or multiple functions closely representing the same curve.^{29,49} In the current investigation, registered image segments were rotated such that their centroids aligned with the two points where the centerline and wire intersect the segment's orthogonal plane; a similar procedure was implemented by Wahle *et al.*⁶⁴ Finally, it can be difficult to obtain a complete picture of the lumen cross-sectional shape from biplane angiography^{40,55} thus hindering attempts to use lumen-matching algorithms. The methods presented in the current investigation produce a single wire pathway and rotational

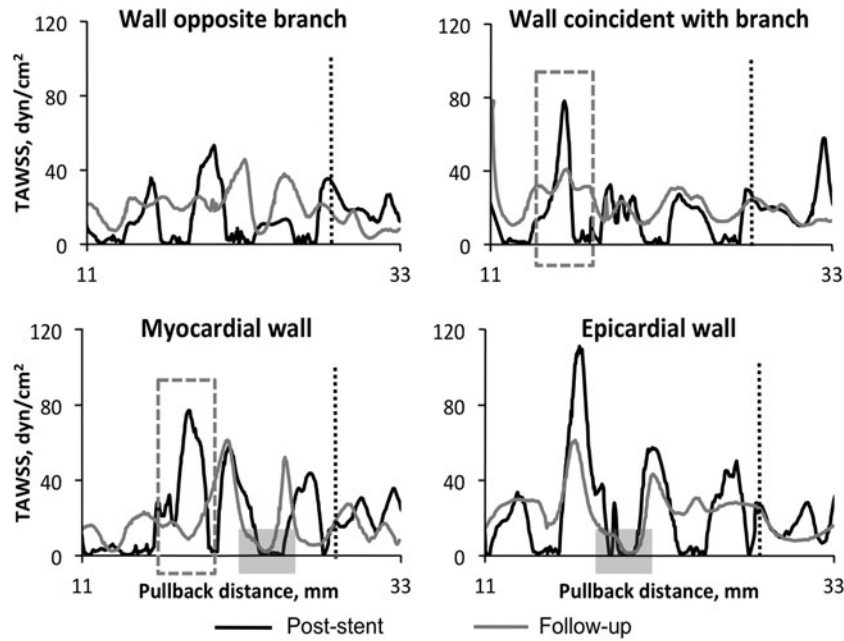


FIGURE 10. TAWSS (dyn/cm^2) along the length of the LCX queried at four circumferential regions for post-stent (black) and follow-up (grey) conditions. The vertical dashed line indicates the proximal end of the stent (the distal end is at 11 mm). In most cases, low TAWSS next to stent struts is alleviated after the follow-up period. However on the myocardial wall at 24 mm and the epicardial wall at 20 mm (gray highlighted boxes), two regions of localized vessel curvature, TAWSS remains at low values. High TAWSS in intrastent regions at post-stent decreased at follow-up (grey dashed boxes).

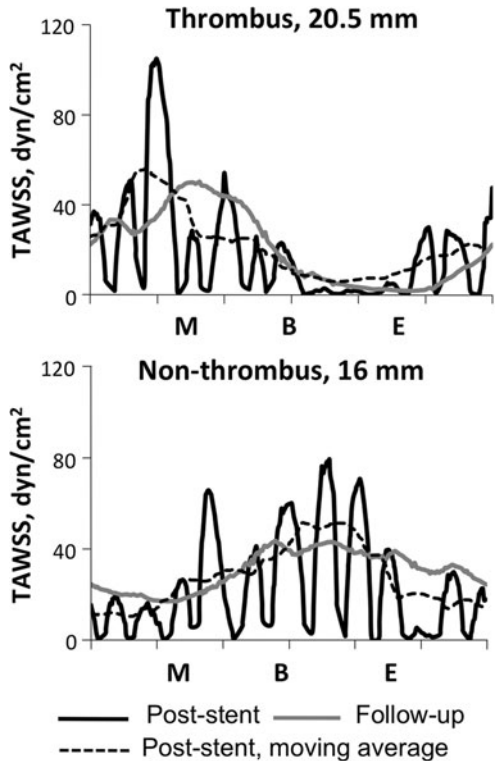


FIGURE 11. TAWSS (dyn/cm^2) at two high WSS longitudinal locations for post-stent (black) and follow-up (grey) conditions. Superimposed (dashed line) is a moving average of the post-stent TAWSS with an averaging window size equal to the intrastent dimension. M: myocardial; B: branch (OM2); E: endocardial.

orientation of segments on this pathway that can be determined regardless of cross-sectional shape, wire location, or presence of pathological landmarks.

Wire Conformation Reconstruction Parameters

The wire pathway reconstruction process was designed using parameters provided by Schafer *et al.*⁵³ to ensure a unique pathway. In addition to a suggested minimum tortuosity threshold of 1.2 exceeded in the current investigation, they also found that 16 planes sufficed for a phantom of 229 mm length and 4.5 mm diameter. Therefore, the 33 planes used in this investigation were adequate to define the LCX with length 107 mm and diameter ~ 2.5 mm. Finally, Schafer *et al.* suggests that 13 candidate points per plane are sufficient to estimate guidewire position with minimal deviation from its actual location. Explicit determination of the wire locations at branch landmarks from registration of OCT images against CT data and the inclusion of a refinement step ensured the accuracy of the wire pathway determined by these methods.

To further determine the influence of the number of candidate points in each plane on the wire pathway, the method was also performed with 41 points per plane, the maximum chosen by Schafer *et al.*⁵³ The root-mean-square (RMS) distance was calculated

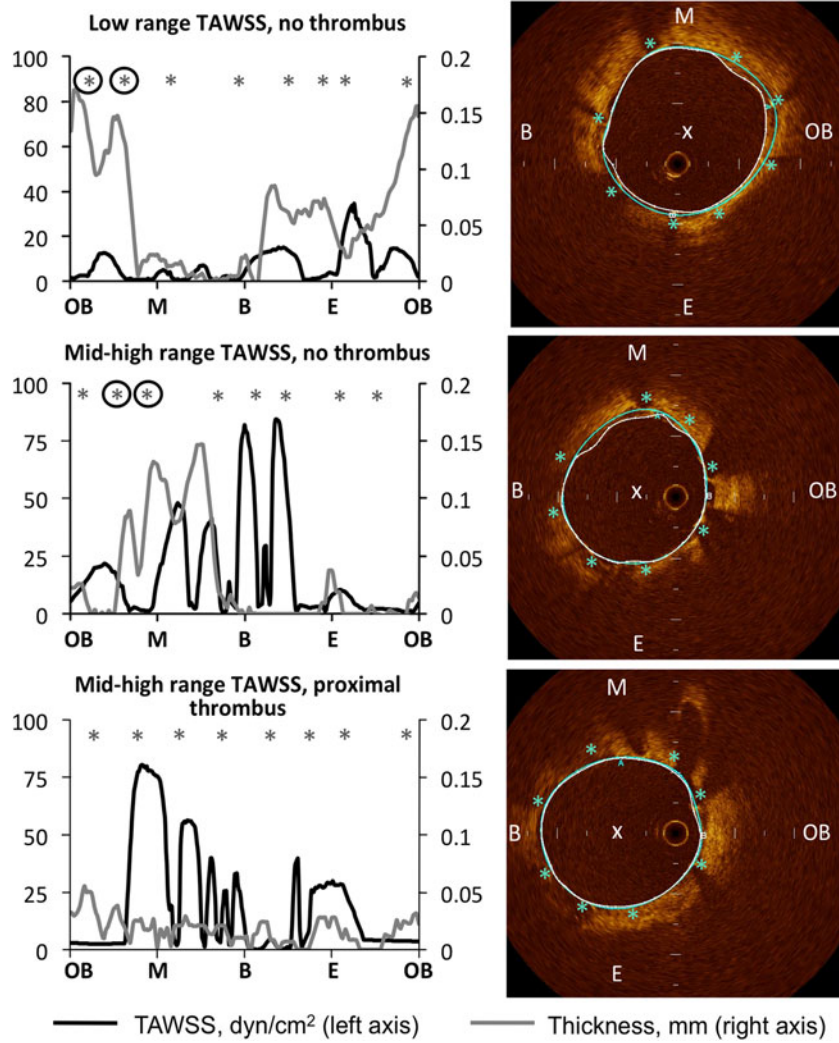


FIGURE 12. TAWSS at post-stent (black) and intimal thickness at follow-up (grey) as determined from post-stent CFD simulation results and follow-up OCT images (right). Stent locations are marked with an asterisk and lumen centroids are marked with a white 'x'. Two cross-sections in non-thrombus areas show measurable growth at areas of low WSS at stent struts (top and middle, circled). Conversely a cross-section that included the proximal end of the thrombus showed minimal growth at follow-up (bottom), as did the non-thrombus cross-section with high WSS (middle). M: myocardial; B: branch (OM2); E: endocardial; OB: opposite side from branch.

between pathways determined with 13 vs. 41 points as

$$\sqrt{\frac{1}{N} \sum_{i=1}^N (d_{13}(i) - d_{41}(i))^2}$$

where $d(i)$ are distances between corresponding points i between the two pathways and N is the total number of points. The RMS distance within the modeled region was calculated to be 0.08, though for the entire pathway extending beyond the modeled region the RMS distance was 0.39. The two pathways placed within the context of the solid model are shown in Fig. 13a. Deviations of the two pathways in the proximal and

distal vessel regions can be seen, but these regions were used solely to ensure sufficient tortuosity for the pathway determination and a similar pattern of deviation at pathway endpoints was found by Schafer *et al.*⁵³ The percentages of the vessel diameter (~2.5 mm) that the RMS distances occupied were 3% for the modeled region and 15% for the entire pathway. It is important to note that the percent in the modeled region is lower than the 6 and 4% for the 4.5 and 3.6 mm diameter phantoms used by Schafer *et al.*⁵³ A visual inspection of the two pathways within the modeled region corroborated the quantitative analysis. The close match in the modeled region but greater deviation outside of it may indicate that the



FIGURE 13. (a) Solid model with wire pathways reconstructed from 13 (black) and 41 (gray) candidate points per orthogonal plane. Distributions of mean WSS are nearly identical for vessels reconstructed with segments registered on pathways using 13 (b) as compared to 41 (c) candidate points.

current method of using the wire-to-centroid distance from OCT images for wire location and the refinement step helped constrain the pathway, while extending the pathway to achieve sufficient tortuosity ensured its uniqueness in the region of interest.

Vessels reconstructed with segments registered on pathways resulting from 13 vs. 41 candidate points were compared in a CFD analysis to further confirm that the number of candidate points per plane does not adversely affect model building. Visible differences between the two models were negligible despite several segments at identical registration points having a slight angular shift, the largest of which was 4° . The two models were then each subjected to a CFD simulation with mean flow in order to compare WSS results (Figs. 13b and 13c). Greater than 99% of the surface area showed less than 47% error between the two models, the value of error historically attributed to geometric influences in patient-specific model creation.³⁷ The percentage of the vessel surface exposed to low WSS ($<4 \text{ dyn/cm}^2$) was 3% in both models and average WSS distributions across the entire surface area for the two models differed by just 1%, further substantiating the claim of similarity between the two models. In short, the findings from this analysis confirm the parameters provided by Schafer *et al.*⁵³ and

are sufficient for patient-specific model creation when combined with the methods described here.

Assessment of WSS Indices and Correlation with NT

The 3D reconstructed LCX artery models of post-stent and follow-up flow domains presented here facilitate the correlation of local WSS indices with NT as observed in OCT images. Results for TAWSS and OSI follow patterns described previously.^{30,34,35} For example, the amount of the lumen exposed to low TAWSS is higher for the stented model than the follow-up model, since low TAWSS is generally alleviated after tissue grows around and atop stent struts during the follow-up period, and areas of high TAWSS inhibit NT even in cases of established atherosclerosis. These results obtained from applying the current methods further show that low TAWSS and high OSI can remain in areas of vessel curvature. It can be seen from longitudinal and circumferential quantification methods that there is a diminishing of WSS gradients from stenting during the follow-up period, i.e. TAWSS appears to average out to what is perhaps a homeostatic level as surmised by observing the moving averages shown in Fig. 11. These findings are consistent with what has been observed in previous studies.^{12,18,67}

The high resolution of OCT images offers the ability to quantify arterial response within the stented region and hypothesize possible relationships between TAWSS post-stenting and NT at follow-up that can be analyzed in greater detail in future studies. It is interesting to note that neointimal growth was minimal at the proximal edge of the thrombus where high TAWSS was observed. The high TAWSS in this area may also correlate with the significant decrease in size of the thrombus. In contrast, several non-thrombotic areas of TAWSS near 0 dyn/cm^2 at the stent struts correlate with the highest growth at those cross-sections. Future studies of larger populations of patients are required to test the hypothesized relationships resulting from this initial investigation.

Limitations

The current results should be interpreted within the constraints of several potential limitations. In this retrospective case study, CT data had been acquired only before stenting. This allowed us to confirm the location of thrombus and general anatomical landmarks, but may have slightly impacted centerline determination in the thrombus region. Future studies designed to apply these methods in a larger population could be designed to include CT immediately after stenting and possibly at follow-up as well. Although

stent artifact has been shown to hinder stent assessability with CT, we expect it has minimal impact on centerline determination and proximal and distal artery reconstruction.^{2,54} The methods for OCT imaging wire pathway determination need only an approximate centerline, so in cases where CT is not available or radiation is an issue, they could still be used in conjunction with other imaging modalities to recreate the artery using OCT images with improved resolution over IVUS. It should be noted as well that newer frequency-domain OCT systems have pullback speeds 10–20 times greater than the time-domain system used for this study.^{22,59} The faster system would undoubtedly allow for more efficient data acquisition, but the methodology proposed here should be applicable regardless of the speed of the OCT system used. Currently OCT is not routine coronary intervention, but it is being incorporated into clinical procedures more frequently, potentially making the methods presented here amenable to usage in larger patient populations. Finally, although NT can be quantified after follow-up in the stented region, it is not entirely clear from OCT if growth observed at follow-up is immature intimal tissue as opposed to thrombus, since the intensity is lower than what would be expected for neointimal growth. However, the indication that the growth may correlate with low WSS at stent struts motivates future studies to apply these methods with a larger patient population, at which time the thickness will be investigated in more detail.

In summary, the current investigation describes a method for 3D patient-specific coronary artery reconstruction using the favorable spatial resolution of OCT while exploiting a current implementation of graph theory techniques. The reconstructed stented model presented in this study included a flexed stent created with novel methods that closely follows vessel geometry. TAWSS and OSI obtained from CFD simulations performed using these models are consistent with earlier studies, and the use of OCT allows us to also quantify NT directly from images for comparison with these WSS results. These reconstruction methods may be used in future studies with a larger patient population to further extract precise local information correlating WSS with NT.

ACKNOWLEDGMENTS

This work is supported by a Translational Opportunity Grant of the Pilot and Collaborative Clinical and Translational Research Grants program from the Clinical and Translational Science Institute of Southeastern Wisconsin (to JFL) and a Junior Faculty

Award from the American Diabetes Association (to JFL). Computational support for this work was made possible by NSF grants CTS-0521602 and OCI-0923037 and assistance from Dr. Daniel Rowe, Marquette University. Dr. Bon-Kwon Koo is the recipient of a research grant from the CardioVascular Research Foundation (CVRF), Korea.

REFERENCES

- ¹Alderliesten, T., P. A. N. Bosman, and W. J. Niessen. Towards a real-time minimally-invasive vascular intervention simulation system. *IEEE Trans. Med. Imaging* 26(1):128–132, 2007.
- ²Andreini, D., G. Pontone, S. Mushtaq, M. Pepi, and A. L. Bartorelli. Multidetector computed tomography coronary angiography for the assessment of coronary in-stent restenosis. *Am. J. Cardiol.* 105(5):645–655, 2010. doi:[10.1016/j.amjcard.2009.10.046](https://doi.org/10.1016/j.amjcard.2009.10.046).
- ³Antiga, L., and D. A. Steinman. Robust and objective decomposition and mapping of bifurcating vessels. *IEEE Trans. Med. Imaging* 23(6):704–713, 2004.
- ⁴Arfsten, G. *Mathematical Methods for Physicists*. San Diego, CA: Academic, 1985.
- ⁵Barlis, P., and J. M. Schmitt. Current and future developments in intracoronary optical coherence tomography imaging. *EuroIntervention* 4(4):529–533, 2009.
- ⁶Braunwald, E., D. P. Zipes, and P. Libby. *Heart Disease: A Textbook of Cardiovascular Medicine* (6th ed.). W.B. Saunders, 2001.
- ⁷De Santis, G., P. Mortier, M. De Beule, P. Segers, P. Verdonck, and B. Verheghe. Patient-specific computational fluid dynamics: structured mesh generation from coronary angiography. *Med. Biol. Eng. Comput.* 48(4):371–380, 2010. doi:[10.1007/s11517-010-0583-4](https://doi.org/10.1007/s11517-010-0583-4).
- ⁸Dijkstra, J., G. Koning, and J. Reiber. Quantitative measurements in IVUS images. *Int. J. Cardiac Imaging* 15:513–522, 1999.
- ⁹Evans, J. L., K. H. Ng, S. G. Wiet, M. J. Vonesh, W. B. Burns, M. G. Radvany, *et al.* Accurate three-dimensional reconstruction of intravascular ultrasound data. Spatially correct three-dimensional reconstructions. *Circulation* 93(3):567–576, 1996.
- ¹⁰Finn, A. V., G. Nakazawa, M. Joner, F. D. Kolodgie, E. K. Mont, H. K. Gold, *et al.* Vascular responses to drug eluting stents: importance of delayed healing. *Arterioscler. Thromb. Vasc. Biol.* 27(7):1500–1510, 2007.
- ¹¹Gijsen, F. J., F. Migliavacca, S. Schievano, L. Soccì, L. Petrini, A. Thury, *et al.* Simulation of stent deployment in a realistic human coronary artery. *Biomed. Eng. Online* 7:23, 2008. doi:[10.1186/1475-925x-7-23](https://doi.org/10.1186/1475-925x-7-23).
- ¹²Gijsen, F. J., R. M. Oortman, J. J. Wentzel, J. C. Schuurbijs, K. Tanabe, M. Degertekin, *et al.* Usefulness of shear stress pattern in predicting neointima distribution in sirolimus-eluting stents in coronary arteries. *Am. J. Cardiol.* 92(11):1325–1328, 2003.
- ¹³Gilbert, J., J. Raboud, and B. Zinman. Meta-analysis of the effect of diabetes on restenosis rates among patients receiving coronary angioplasty stenting. *Diabetes Care* 27(4):990–994, 2004.

- ¹⁴Goubergrits, L., E. Wellnhofer, U. Kertzscher, K. Affeld, C. Petz, and H. C. Hege. Coronary artery WSS profiling using a geometry reconstruction based on biplane angiography. *Ann. Biomed. Eng.* 37(4):682–691, 2009. doi:10.1007/s10439-009-9656-7.
- ¹⁵Gow, B. S., D. Schonfeld, and D. J. Patel. The dynamic elastic properties of the canine left circumflex coronary artery. *J. Biomech.* 7(5):389–395, 1974. doi:10.1016/0021-9290(74)90001-3.
- ¹⁶Gundert, T. J., S. C. Shadden, A. R. Williams, B. K. Koo, J. A. Feinstein, and J. F. Ladisa. A rapid and computationally inexpensive method to virtually implant current and next-generation stents into subject-specific computational fluid dynamics models. *Ann. Biomed. Eng.* 2011. doi:10.1007/s10439-010-0238-5.
- ¹⁷Hamuro, M., J. C. Palmaz, E. A. Sprague, C. Fuss, and J. Luo. Influence of stent edge angle on endothelialization in an in vitro model. *J. Vasc. Interv. Radiol.* 12(5):607–611, 2001.
- ¹⁸He, Y., N. Duraiswamy, A. O. Frank, and J. E. Moore. Blood flow in stented arteries: a parametric comparison of strut design patterns in three dimensions. *J. Biomech. Eng.* 127(4):637–647, 2005.
- ¹⁹He, X., and D. N. Ku. Pulsatile flow in the human left coronary artery bifurcation: average conditions. *J. Biomech. Eng.* 118:74–82, 1996.
- ²⁰Holmes, Jr., D. R., D. J. Kereiakes, S. Garg, P. W. Serruys, G. J. Dehmer, S. G. Ellis, *et al.* Stent thrombosis. *J. Am. Coll. Cardiol.* 56(17):1357–1365, 2010. doi:10.1016/j.jacc.2010.07.016.
- ²¹Iakovou, I., T. Schmidt, E. Bonizzoni, L. Ge, G. M. Sangiorgi, G. Stankovic, *et al.* Incidence, predictors, and outcome of thrombosis after successful implantation of drug-eluting stents. *JAMA* 293(17):2126–2130, 2005.
- ²²Imola, F., M. T. Mallus, V. Ramazzotti, A. Manzoli, A. Pappalardo, A. Di Giorgio, *et al.* Safety and feasibility of frequency domain optical coherence tomography to guide decision making in percutaneous coronary intervention. *EuroIntervention* 6(5):575–581, 2010. doi:EIJV615A97[pil]10.4244/EIJV615A97.
- ²³Joner, M., G. Nakazawa, A. V. Finn, S. C. Quee, L. Coleman, E. Acapado, *et al.* Endothelial cell recovery between comparator polymer-based drug-eluting stents. *J. Am. Coll. Cardiol.* 52(5):333–342, 2008. doi:10.1016/j.jacc.2008.04.030.
- ²⁴Kern, M. Biplane coronary angiography: an old dog with new tricks. *Cath. Lab. Digest.* 2009.
- ²⁵Konings, M. K., E. B. van de Kraats, T. Alderliesten, and W. J. Niessen. Analytical guide wire motion algorithm for simulation of endovascular interventions. *Med. Biol. Eng. Comput.* 41(6):689–700, 2003.
- ²⁶Kotani, J., M. Awata, S. Nanto, M. Uematsu, F. Oshima, H. Minamiguchi, *et al.* Incomplete neointimal coverage of sirolimus-eluting stents: angioscopic findings. *J. Am. Coll. Cardiol.* 47(10):2108–2111, 2006.
- ²⁷Krams, R., J. J. Wentzel, J. A. F. Oomen, R. Vinke, J. C. H. Schuurbijs, P. J. de Feyter, *et al.* Evaluation of endothelial shear stress and 3D geometry as factors determining the development of atherosclerosis and remodeling in human coronary arteries in vivo : combining 3D reconstruction from angiography and IVUS (ANGUS) with computational fluid dynamics. *Arterioscler. Thromb. Vasc. Biol.* 17(10):2061–2065, 1997.
- ²⁸Kuchulakanti, P. K., W. W. Chu, R. Torguson, P. Ohlmann, S. W. Rha, L. C. Clavijo, *et al.* Correlates and long-term outcomes of angiographically proven stent thrombosis with sirolimus- and paclitaxel-eluting stents. *Circulation* 113(8):1108–1113, 2006.
- ²⁹Laban, M., J. A. Oomen, C. J. Slager, J. J. Wentzel, R. Krams, J. C. H. Schuurbijs, *et al.*, editors. ANGUS: a new approach to three-dimensional reconstruction of coronary vessels by combined use of angiography and intravascular ultrasound. *Computers in Cardiology*, 10–13 Sep. 1995.
- ³⁰LaDisa, Jr., J. F., M. Bowers, L. Harmann, R. Prost, A. V. Doppalapudi, T. Mohyuddin, *et al.* Time-efficient patient-specific quantification of regional carotid artery fluid dynamics and spatial correlation with plaque burden. *Med. Phys.* 37(2):784–792, 2010.
- ³¹LaDisa, Jr., J. F., I. Guler, L. E. Olson, D. A. Hettrick, J. R. Kersten, D. C. Warltier, *et al.* Three-dimensional computational fluid dynamics modeling of alterations in coronary wall shear stress produced by stent implantation. *Ann. Biomed. Eng.* 31(8):972–980, 2003.
- ³²LaDisa, Jr., J. F., D. A. Hettrick, L. E. Olson, I. Guler, E. R. Gross, T. T. Kress, *et al.* Stent implantation alters coronary artery hemodynamics and wall shear stress during maximal vasodilation. *J. Appl. Physiol.* 93(6):1939–1946, 2002. doi:10.1152/jappphysiol.00544.2002.
- ³³LaDisa, Jr., J. F., L. E. Olson, I. Guler, D. A. Hettrick, S. H. Audi, J. R. Kersten, *et al.* Stent design properties and deployment ratio influence indexes of wall shear stress: a three-dimensional computational fluid dynamics investigation within a normal artery. *J. Appl. Physiol.* 97:424–430, 2004.
- ³⁴LaDisa, Jr., J. F., L. E. Olson, I. Guler, D. A. Hettrick, J. R. Kersten, D. C. Warltier, *et al.* Circumferential vascular deformation after stent implantation alters wall shear stress evaluated using time-dependent 3D computational fluid dynamics models. *J. Appl. Physiol.* 98(3):947–957, 2005.
- ³⁵LaDisa, Jr., J. F., L. E. Olson, R. C. Molthen, D. A. Hettrick, P. F. Pratt, M. D. Hardel, *et al.* Alterations in wall shear stress predict sites of neointimal hyperplasia after stent implantation in rabbit iliac arteries. *Am. J. Physiol. Heart Circ. Physiol.* 288(5):H2465–H2475, 2005.
- ³⁶Leaman, D., R. Brower, G. Meester, P. Serruys, and M. van den Brand. Coronary artery atherosclerosis: severity of the disease, severity of angina pectoris and compromised left ventricular function. *Circulation* 63(2):285–299, 1981.
- ³⁷Lee, S. W., and D. A. Steinman. On the relative importance of rheology for image-based CFD models of the carotid bifurcation. *J. Biomech. Eng.* 129(2):273–278, 2007. doi:10.1115/1.2540836.
- ³⁸Lloyd-Jones, D., R. J. Adams, T. M. Brown, M. Carnethon, S. Dai, G. De Simone, *et al.* Heart disease and stroke statistics-2010 update: a report from the American Heart Association. *Circulation* 121(7):e46–e215, 2010. doi:10.1161/circulationaha.109.192667.
- ³⁹Malek, A. M., S. L. Alper, and S. Izumo. Hemodynamic shear stress and its role in atherosclerosis. *JAMA* 282(21):2035–2042, 1999.
- ⁴⁰Marquering, H., J. Dijkstra, Q. Besnehard, J. Duth'e, J. Schuijf, J. Bax *et al.*, editors. Coronary CT angiography: IVUS image fusion for quantitative plaque and stenosis analyses. Society of Photo-Optical Instrumentation Engineers (SPIE) Conference Series, 2008.
- ⁴¹Moses, J. W., M. B. Leon, J. J. Popma, P. J. Fitzgerald, D. R. Holmes, C. O'Shaughnessy, *et al.* Sirolimus-eluting stents versus standard stents in patients with stenosis in a native coronary artery. *N. Engl. J. Med.* 349(14):1315–1323, 2003.

- ⁴²Muller, J., O. Sahni, X. Li, K. E. Jansen, M. S. Shephard, and C. A. Taylor. Anisotropic adaptive finite element method for modelling blood flow. *Comput. Meth. Biomech. Biomed. Eng.* 8(5):295–305, 2005. doi:[10.1080/10255840500264742](https://doi.org/10.1080/10255840500264742).
- ⁴³Murata, A., D. Wallace-Bradley, A. Tellez, C. Alviar, M. Aboodi, A. Sheehy, *et al.* Accuracy of optical coherence tomography in the evaluation of neointimal coverage after stent implantation. *JACC Cardiovasc. Imaging* 3(1):76–84, 2010. doi:[S1936-878X\(09\)00757-8\[pii\]10.1016/j.jcmg.2009.09.018](https://doi.org/10.1016/j.jcmg.2009.09.018).
- ⁴⁴Myers, J. G., J. A. Moore, M. Ojha, K. W. Johnston, and C. R. Ethier. Factors influencing blood flow patterns in the human right coronary artery. *Ann. Biomed. Eng.* 29:109–120, 2001.
- ⁴⁵Nissen, S. E., and P. Yock. Intravascular ultrasound: novel pathophysiological insights and current clinical applications. *Circulation* 103(4):604–616, 2001.
- ⁴⁶Otake, H., J. Shite, J. Ako, T. Shinke, Y. Tanino, D. Ogasawara, *et al.* Local determinants of thrombus formation following sirolimus-eluting stent implantation assessed by optical coherence tomography. *J. Am. Coll. Cardiol. Interv.* 2(5):459–466, 2009. doi:[10.1016/j.jcin.2009.03.003](https://doi.org/10.1016/j.jcin.2009.03.003).
- ⁴⁷Papafaklis, M. I., C. V. Bourantas, P. E. Theodorakis, C. S. Katsouras, K. K. Naka, D. I. Fotiadis, *et al.* The effect of shear stress on neointimal response following sirolimus- and paclitaxel-eluting stent implantation compared with bare-metal stents in humans. *J. Am. Coll. Cardiol. Interv.* 3(11):1181–1189, 2010. doi:[10.1016/j.jcin.2010.08.018](https://doi.org/10.1016/j.jcin.2010.08.018).
- ⁴⁸Prause, G. P., S. C. DeJong, C. R. McKay, and M. Sonka. Towards a geometrically correct 3-D reconstruction of tortuous coronary arteries based on biplane angiography and intravascular ultrasound. *Int. J. Cardiac Imaging* 13(6):451–462, 1997.
- ⁴⁹Prause, G. P. M., S. C. DeJong, C. R. McKay, and M. Sonka, editors. Geometrically correct 3-D reconstruction of coronary wall and plaque: combining biplane angiography and intravascular ultrasound. *Computers in Cardiology*, 8–11 Sep. 1996.
- ⁵⁰Redwood, S., N. Curzen, and M. Thomas. *Oxford Textbook of Interventional Cardiology*. Oxford: Oxford University Press, 2010.
- ⁵¹Sahni, O., J. Müller, K. E. Jansen, M. S. Shephard, and C. A. Taylor. Efficient anisotropic adaptive discretization of the cardiovascular system. *Comput. Meth. Appl. Mech. Eng.* 195(41–43):5634–5655, 2006. doi:[10.1016/j.cma.2005.10.018](https://doi.org/10.1016/j.cma.2005.10.018).
- ⁵²Schafer, S., K. R. Hoffmann, P. B. Noel, C. N. Ionita, and J. Dmochowski. Evaluation of guidewire path reproducibility. *Med. Phys.* 35(5):1884–1892, 2008.
- ⁵³Schafer, S., V. Singh, P. B. Noel, A. M. Walczak, J. Xu, and K. R. Hoffmann. Real-time endovascular guidewire position simulation using shortest path algorithms. *Int. J. Comput. Assist. Radiol. Surg.* 4(6):597–608, 2009. doi:[10.1007/s11548-009-0385-z](https://doi.org/10.1007/s11548-009-0385-z).
- ⁵⁴Sheth, T., J. D. Dodd, U. Hoffmann, S. Abbara, A. Finn, H. K. Gold, *et al.* Coronary stent assessability by 64 slice multi-detector computed tomography. *Catheter. Cardiovasc. Interv.* 69(7):933–938, 2007. doi:[10.1002/ccd.21130](https://doi.org/10.1002/ccd.21130).
- ⁵⁵Slager, C. J., J. J. Wentzel, J. C. H. Schuurbijs, J. A. F. Oomen, J. Kloet, R. Krams, *et al.* True 3-dimensional reconstruction of coronary arteries in patients by fusion of angiography and IVUS (ANGUS) and its quantitative validation. *Circulation* 102(5):511–516, 2000.
- ⁵⁶Stergopoulos, N., J. J. Meister, and N. Westerhof. Simple and accurate way for estimating total and segmental arterial compliance: the pulse pressure method. *Ann. Biomed. Eng.* 22(4):392–397, 1994.
- ⁵⁷Stergopoulos, N., P. Segers, and N. Westerhof. Use of pulse pressure method for estimating total arterial compliance in vivo. *Am. J. Physiol. Heart Circ. Physiol.* 276(2 Pt 2):H424–H428, 1999.
- ⁵⁸Subramanian, K. R., M. J. Thubrikar, B. Fowler, M. T. Mostafavi, and M. W. Funk. Accurate 3D reconstruction of complex blood vessel geometries from intravascular ultrasound images: in vitro study. *J. Med. Eng. Technol.* 24(4):131–140, 2000.
- ⁵⁹Takarada, S., T. Imanishi, Y. Liu, H. Ikejima, H. Tsujioka, A. Kuroi, *et al.* Advantage of next-generation frequency-domain optical coherence tomography compared with conventional time-domain system in the assessment of coronary lesion. *Catheter. Cardiovasc. Interv.* 75(2):202–206, 2010. doi:[10.1002/ccd.22273](https://doi.org/10.1002/ccd.22273).
- ⁶⁰Tang, B. T., C. P. Cheng, M. T. Draney, N. M. Wilson, P. S. Tsao, R. J. Herfkens, *et al.* Abdominal aortic hemodynamics in young healthy adults at rest and during lower limb exercise: quantification using image-based computer modeling. *Am. J. Physiol. Heart Circ. Physiol.* 291(2):H668–H676, 2006.
- ⁶¹Taylor, C. A., and D. A. Steinman. Image-based modeling of blood flow and vessel wall dynamics: applications, methods and future directions: Sixth International Bio-Fluid Mechanics Symposium and Workshop, March 28–30, 2008 Pasadena, California. *Ann. Biomed. Eng.* 38(3):1188–1203, 2010. doi:[10.1007/s10439-010-9901-0](https://doi.org/10.1007/s10439-010-9901-0).
- ⁶²Van Huis, G. A., P. Sipkema, and N. Westerhof. Coronary input impedance during cardiac cycle as determined by impulse response method. *Am. J. Physiol.* 253(2 Pt 2):H317–H324, 1987.
- ⁶³Vignon-Clementel, I. E., C. A. Figueroa, K. E. Jansen, and C. A. Taylor. Outflow boundary conditions for three-dimensional finite element modeling of blood flow and pressure in arteries. *Comput. Methods Appl. Mech. Eng.* 195:3776–3796, 2006.
- ⁶⁴Wahle, A., G. P. M. Prause, C. Von Birgelen, R. Erbel, and M. Sonka. Fusion of angiography and intravascular ultrasound in vivo: establishing the absolute 3-D frame orientation. *IEEE Trans. Biomed. Eng.* 46(10):1176–1180, 1999.
- ⁶⁵Wentzel, J. J., F. J. Gijsen, J. C. Schuurbijs, A. F. van der Steen, and P. W. Serruys. The influence of shear stress on in-stent restenosis and thrombosis. *EuroIntervention* 4(Suppl C):C27–C32, 2008.
- ⁶⁶Wentzel, J. J., F. J. H. Gijsen, N. Stergiopoulos, P. W. Serruys, C. J. Slager, and R. Krams. Shear stress, vascular remodeling and neointimal formation. *J. Biomech.* 36(5):681–688, 2003. doi:[10.1016/s0021-9290\(02\)00446-3](https://doi.org/10.1016/s0021-9290(02)00446-3).
- ⁶⁷Wentzel, J. J., R. Krams, J. C. H. Schuurbijs, J. A. Oomen, J. Kloet, W. J. van der Giessen, *et al.* Relationship between neointimal thickness and shear stress after wall-stent implantation in human coronary arteries. *Circulation* 103:1740–1745, 2001.
- ⁶⁸Westerhof, N., N. Stergiopoulos, and M. I. M. Noble. *Snapshots of Hemodynamics: An Aid for Clinical Research and Graduate Education*. New York: Springer, 2005.
- ⁶⁹Williams, A. R., B.-K. Koo, T. J. Gundert, P. J. Fitzgerald, and J. LaDisa, Jr. Local hemodynamic changes caused by main branch stent implantation and virtual side branch balloon angioplasty in a representative coronary bifurcation. *J. Appl. Physiol.* 109:532–540, 2010. doi:[10.1152/japplphysiol.00086.2010](https://doi.org/10.1152/japplphysiol.00086.2010).